

Data-driven perspectives on linear stability theory: dataset support and pattern-based N-factor evaluation

Shen'ao Xiao,¹ Wenhui Chang,¹ Hongyuan Hu,¹ Jie Ren,^{1, 2,*} and Xuerui Mao¹

¹*State Key Laboratory of Explosion Science and Safety Protection,
Beijing Institute of Technology, Beijing 100081, China*

²*State Key Laboratory of Environment Characteristics and Effects for Near-space,
Beijing Institute of Technology, Beijing 100081, China*

(Dated: April 18, 2025)

Boundary-layer instability acts as the precursor to the laminar-turbulent transition, influencing both its initiation and spatio-temporal characteristics. In the linear regime, linear stability theory (LST) has proven effective in identifying neutral curves and predicting transition via the N -factor. However, a clear connection between data in Fourier space and physical space has yet to be fully established—despite the latter offering an aggregable dataset that could address the increasing complexity of flow conditions in real-world applications. To investigate this link, we apply LST in the Fourier domain to two representative cases: an incompressible flat-plate boundary layer and its hypersonic counterpart ($Ma = 4.8$), producing baseline data. We then reconstruct the perturbation fields in physical space and introduce various initial disturbances. The evolution and spatial distribution of modal perturbations are visualized across different planes. Next, we utilize a convolutional neural network (CNN) to predict the N -factor based on these visualized perturbation fields. Our results demonstrate that the majority of the absolute errors between CNN predictions and LST calculations remain within ± 0.2 . Moreover, by employing more advanced neural network architectures, we reduce the median prediction error to ± 0.03 , indicating a minimal error for the N -factor. These results highlight the potential of leveraging upstream perturbation amplitude measurements in conjunction with data-driven models to enable real-time prediction of transition onset—with performance and coverage expected to improve further as larger datasets become available.

I. INTRODUCTION

Flow instability bridges laminar flow and the turbulent states that exhibit stochastic and chaotic behavior. Linear stability theory (LST) is widely used in the linear regime to analyze the stability of boundary layer flows, predict transition points, and devise control strategies to delay turbulence onset [1, 2]. Recent developments in LST have expanded its application to high-dimensional baseflows [3], integrated data-driven techniques [4], and addressed non-ideal flow scenarios [5–8].

Flow instability itself encompasses a variety of mechanisms that emerge in different flow conditions, which promote the amplification of perturbations. This study specifically examines the modal growth of boundary layers, which may involve several distinct types of instability. These include the Tollmien-Schlichting (T-S) waves [9] in typical boundary layers, Mack's second mode [10, 11] in hypersonic flows, crossflow vortices [2] frequently observed in three-dimensional boundary layers with favorable pressure gradients, Görtler vortices over concave surfaces [12], and attachment line instability typically found near attachment lines in flows over surfaces such as wings [13]. Additionally, numerous factors influence the boundary layer's response to external disturbances, and as a result, a universally applicable theory of transition remains elusive [14].

The rapid progress in machine learning techniques has opened new possibilities for data-driven analysis in flow stability research. For example, convolutional neural networks (CNNs) have been incorporated into classical linear stability theory (LST) frameworks, enabling the prediction of local disturbance growth rates by learning from boundary layer velocity profiles and perturbation parameters [15]. Another approach used Deep operator networks (DeepONet) to model the evolution of linear instability waves in high-speed boundary layers by mapping upstream disturbances to downstream flow fields, addressing both forward prediction and inverse problems [16]. Expanding on DeepONet, the DeepM&Mnet framework has been proposed to predict flow fields across shock waves [17]. Moreover, in response to engineering needs, surrogate models have been developed to approximate solutions to linear stability equations [18], effectively predicting transition processes in compressible boundary layers.

In machine learning, the availability of standardized datasets has greatly accelerated the development and application of models. For instance, the ImageNet dataset [19] was pivotal in advancing deep learning, particularly

* jie.ren@bit.edu.cn

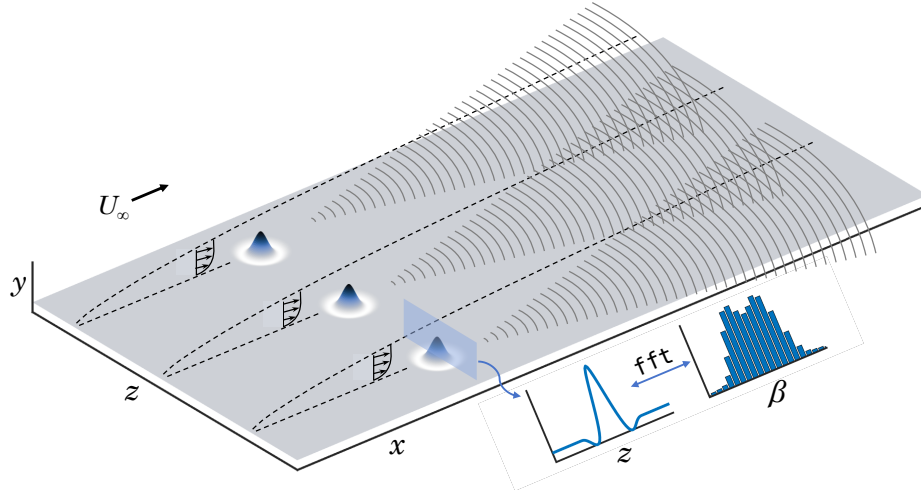


FIG. 1. Illustration of Tollmien–Schlichting wave amplification induced by point sources following a prescribed Fourier distribution. A central cut highlights the perturbation distribution in both the physical domain (spanwise coordinate z) and the Fourier domain (wavenumber β).



with CNNs' breakthrough performance in the ILSVRC (ImageNet Large Scale Visual Recognition Challenge) [20], marking a significant milestone in deep learning for computer vision. Similarly, the LibriSpeech dataset [21] has driven advancements in speech recognition, providing vital resources for optimizing recognition models. The SQuAD dataset [22] has made substantial contributions to Natural Language Processing (NLP), offering a question-answering framework for machine reading comprehension tasks. Therefore, well-curated, high-quality datasets can profoundly transform research across various domains by enabling more efficient model development and enhancing the accuracy and applicability of predictive methods.

Building on this inspiration, flow instability, being deterministic relative to turbulence, stands to benefit from a similar approach. A dedicated database could enhance traditional stability analyses and provide a foundation for identifying and predicting critical instability features using machine learning, even with limited observational data. This approach would facilitate the rapid reconstruction of flow fields across different parameters. Additionally, the development of turbulence databases [23] serves as valuable tools for recognizing turbulence patterns [24] and validating models [25]. However, the vast size of turbulence data from a single case, reaching over 100 terabytes of storage, presents challenges in blanket data processing. Additionally, the inherent randomness of turbulence complicates the precise reproduction of instantaneous behaviors, leading researchers to focus primarily on statistical quantities [26].

From a data-driven perspective, we extend LST from Fourier space to physical space and reconstruct the perturbation and flow fields based on the characteristics of external disturbance sources. The data in physical space will capture essential flow phenomena and serve as the foundation for a specialized database on flow instability. We then apply machine learning techniques to predict the N -factor using observables extracted from the data. The rest of the paper is organized as follows: Section II introduces the problem and the methods used; Section III presents the results in both Fourier and physical spaces, discusses the characteristics of disturbances, and uses machine learning methods to predict the N -factor of the flow; Section IV concludes the paper.

II. METHOD

This study considers the linear regime of perturbation growth in a flat-plate boundary layer. The stability diagram is first obtained from LST which provides a dataset in Fourier space for the growth of modal perturbations. As illustrated in Figure 1, when small-amplitude point-source sinusoidal disturbances are introduced, the downstream perturbations grow in accordance with predictions from LST. By matching Fourier coefficients, the influence of different external disturbances on perturbation patterns can be incorporated. The flow evolution is then characterized using planar field visualizations, from which a flow instability dataset is established in physical space. Leveraging this dataset in conjunction with key flow parameters, a data-driven framework is proposed to enable rapid and accurate prediction of the N -factor.

A. Linear stability theory

LST is based on the linearization of the Navier-Stokes (N-S) equations to analyze the growth or decay of small perturbations, $\tilde{\mathbf{q}}$, superimposed on a laminar base flow, \mathbf{Q} . The instantaneous flow field is given by

$$\mathbf{q}(x, y, z, t) = \mathbf{Q}(x, y) + \tilde{\mathbf{q}}(x, y, z, t). \quad (1)$$

The vectors \mathbf{q} , \mathbf{Q} and $\tilde{\mathbf{q}}$ in (1) encompass the fundamental flow variables, consisting of five components for compressible or four for incompressible flows. By introducing the Fourier ansatz:

$$\tilde{\mathbf{q}}(x, y, z, t) = \hat{\mathbf{q}}(y) \exp(i\alpha x + i\beta z - i\omega t) + \text{complex conjugate}, \quad (2)$$

the linearised N-S equations for $\hat{\mathbf{q}}(x, y, z, t)$ are formulated as

$$\mathbf{L}(\mathbf{Q}, \alpha, \beta, \omega, Re, Ma) \hat{\mathbf{q}} = 0, \quad (3)$$

where α and β denote the streamwise and spanwise wavenumbers, respectively, and ω represents the perturbation frequency. The function $\hat{\mathbf{q}}(y)$ describes the shape of the perturbation in Fourier space. The linear operator \mathbf{L} depends on the base flow and the dimensionless numbers characterizing the flow. A detailed expression can be found in previously published works [see for example the appendix of 27]. As a representative example, we consider the spatial stability problem, where α and $\hat{\mathbf{q}}$ are determined by solving equation (3) as an eigenvalue problem. In the non-dimensionalization process, dimensional quantities are indicated using the superscript $(*)^*$. The reference velocity is the free-stream velocity U_∞^* , while the reference length scale is the boundary layer thickness at the inlet, defined as $\delta_0^* = \sqrt{\nu_\infty^* x_0^*/U_\infty^*}$.

B. From Fourier to physical space

Although the Fourier ansatz (2) establishes a connection between the physical and Fourier space, it is inherently a local representation and does not account for the integrated effect of perturbation growth along the streamwise direction. Moreover, the linear nature allows the decoupling of harmonics. To address these issues, the following formula is used to superimpose the disturbances across all spanwise wavenumbers β , multiplied by the initial amplitude matching the external perturbation $\hat{f}(\beta)$, to transform $\hat{\mathbf{q}}$ from Fourier space back to the physical domain.

$$\tilde{\mathbf{q}}(x, y, z, t) = \hat{\mathbf{q}}(y) \sum_{\beta} \left[\hat{f}(\beta) \exp(i\alpha_r(\beta)x + i\beta z - i\omega t + N(\beta, x)) \right] + \text{c.c.} \quad (4)$$

where c.c. denotes complex conjugate, α_r represents the real part of α , while the imaginary part is integrated along the x -direction to calculate the N -factor as:

$$N(\beta, x) = - \int_{x|\alpha_i=0}^x \alpha_i(\beta) dx. \quad (5)$$

The external perturbation functions f can take various forms. For instance, representative functions of point-source type are expressed as:

$$\left. \begin{aligned} f_1(x, z, t) &= (14r^5 - 45r^4 + 50r^3 - 20r^2 + 1) \sin(\omega t + \phi_0); \\ f_2(x, z, t) &= (-40r^6 + 84r^5 - 45r^4 + 1) \sin(\omega t + \phi_0); \\ f_3(x, z, t) &= (-21r^5 + 45r^4 - 25r^3 + 1) \sin(\omega t + \phi_0), \end{aligned} \right\} \quad (6)$$

with:

$$r^2 = \frac{(x - x_c)^2 + (z - z_c)^2}{R^2}, \quad 0 \leq r \leq 1. \quad (7)$$

In (7), x_c and z_c denote the coordinates of the perturbation center, while R represents the perturbation radius. The function is designed to ensure that, at any given moment, the integral of the perturbation across the $x-z$ plane equals zero, thereby preventing the introduction of spurious noise into the flow field. Moreover, the perturbation amplitude reaches its maximum at the disturbance center and gradually decays to zero as the distance from the center increases.

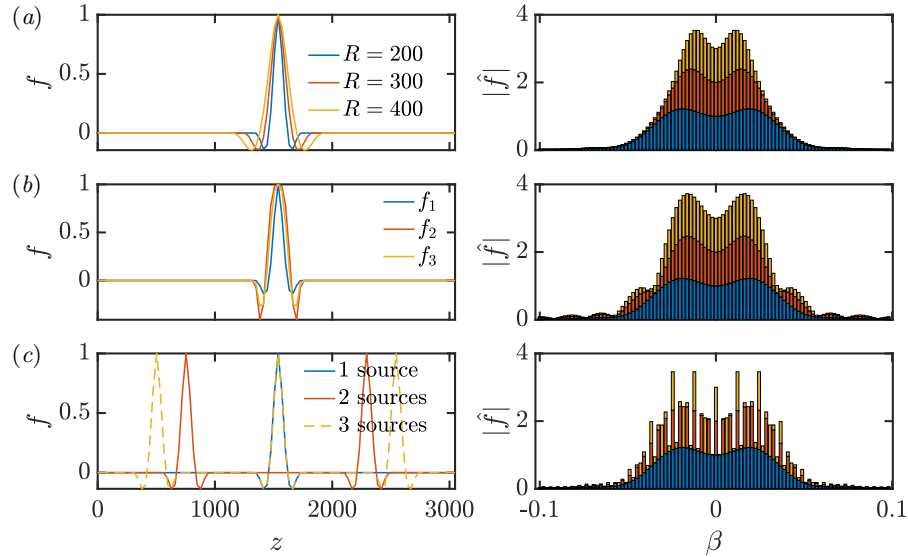


FIG. 2. External perturbation profiles along the z -direction (left columns) and their corresponding normalized Fourier magnitude spectra (right columns, normalized at $\beta = 0$) are shown using stacked bar charts, where values are represented as segments stacked on top of each other within a single bar. (a) Effect of perturbation radius ($f = f_1$, single source); (b) influence of different functional forms ($R = 200$, single source); (c) effect of the number of perturbation sources ($f = f_1$, $R = 200$).

In practice, external point-source disturbances are inherently three-dimensional. The space-averaged spectrum can be considered [28]; however, it does not introduce an essential difference compared to a two-dimensional central slice of the disturbance. From this perspective, this study selects a two-dimensional disturbance slice at x_c , as shown in Figure 1, and a value of 200, 300 or 400 is assigned to R . A Fourier transform is then applied to this slice function, converting it into the wavenumber domain:

$$\hat{f}(\beta_k) = \sum_{n=0}^{N_z-1} f(z_n) e^{-i \frac{2\pi k n}{N_z}}, \quad k = 0, 1, \dots, N_z - 1. \quad (8)$$

The relationship between the wavenumber β_k and k is given as:

$$\beta_k = \frac{2\pi(k - N_z/2)}{N_z \Delta z}, \quad (9)$$

where N_z is the number of sampling points in the spanwise direction. $\hat{f}(\beta_k)$ is then utilized as initial amplitude for the evolution of each wavenumber component of the modal perturbation. As shown in equation (8), the external perturbation configuration $f(z)$ exerts a direct influence on the initial amplitude modulation, as illustrated in Figure 2. As the radius decreases, the physical perturbation becomes increasingly concentrated toward the center, resulting in a broader distribution of Fourier components, as shown in Figure 2(a). The influence of different disturbance functions is illustrated in Figure 2(b), where the Fourier components are modified with comparable magnitudes. Among all factors, the number of disturbance sources exerts the most significant impact. As depicted in panel (c), a scattered pattern appears in the Fourier amplitudes as the number of sources increases.

Physically, the receptivity process leads to proportional modifications in the coefficients of equation (4) [29]. This effect is functionally equivalent to altering the external forcing terms in equation (6). However, such modifications do not compromise the generality of the present framework, as the methodology does not rely on any specific shape or form of the external disturbances.

C. Pattern based prediction using convolutional neural network

The physical field varies depending on the initial conditions and flow parameters. The key feature, the perturbation pattern, is primarily determined by the linear growth rate and dispersion relations. Consequently, instability features can be effectively predicted based on patterns obtained from planar observations.

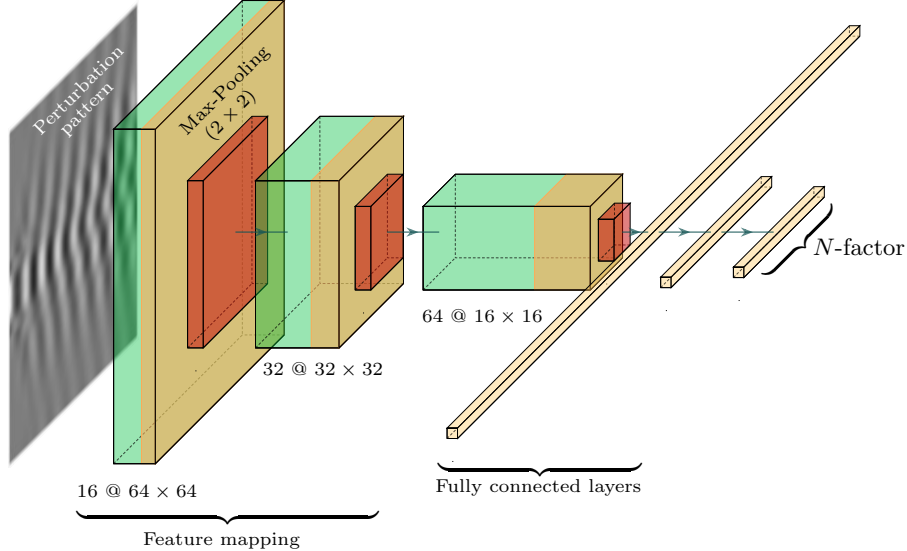


FIG. 3. A schematic diagram of CNN architecture.

Convolutional neural networks (CNNs), a class of deep learning models in machine learning, offer an effective solution for this task. Widely used in computer vision, CNNs uniquely integrate convolutional and pooling layers, enabling robust feature extraction and learning. The convolutional layers apply filters (convolutional kernels) to capture localized features such as edges, corners, and texture patterns from the input data. Meanwhile, pooling layers perform downsampling operations, reducing computational complexity and enhancing model robustness against spatial variations. Finally, fully connected layers process the extracted hierarchical features for classification or regression tasks.

Classic CNN architectures include LeNet, originally developed for handwritten digit recognition with a relatively shallow structure [30]; AlexNet, which significantly advanced image classification accuracy and catalyzed the widespread adoption of deep learning [20]; VGGNet, which deepened the network using stacked small convolutional kernels [31]; and ResNet, which introduced residual connections to address the vanishing gradient problem in deep architectures [32]. Building upon these foundations, CNNs have continued to evolve, giving rise to powerful models such as EfficientNet, which employs a compound scaling strategy to balance network depth, width, and resolution [33], and ConvNeXt, a modern convolutional architecture inspired by Vision Transformer (ViT) design principles that achieves performance on par with or superior to Transformer-based models [34].

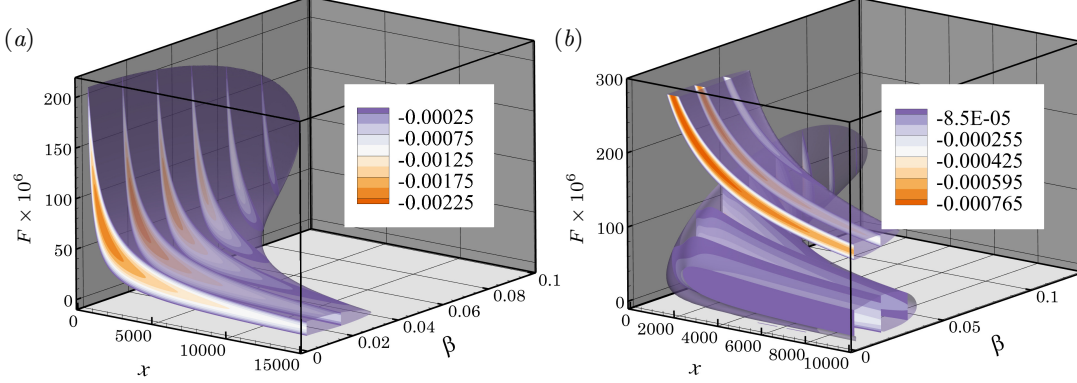
These CNN variants have demonstrated notable success in image classification and provide a solid foundation for the current study on flow instability prediction. In this work, visualizations extracted from three-dimensional flow field data are used as input to the proposed CNN. As shown in Figure 3, the network is trained to predict the corresponding N -factor distributions. The model architecture includes three convolutional layers, each followed by a 2×2 max-pooling layer, and three fully connected layers. The input to the network consists of 128×128 grayscale images that capture flow features under varying external disturbance conditions. The convolutional layers employ 3×3 kernels with 16, 32, and 64 filters, respectively, using a stride of 1 and padding of 1 to preserve spatial dimensions. After feature extraction, the resulting feature maps are flattened and passed through fully connected layers for regression-based prediction. The fully connected layers have 2048, 512, and a final output layer with N_x neurons corresponding to the predicted N -factor.

In engineering applications, the onset of transition is commonly identified when the N -factor reaches a calibrated threshold [9, 35]. The approach introduced in this study enables real-time estimation of the N -factor using observations. Prior to training, the input data are standardized as part of the preprocessing pipeline to ensure consistent scaling.

Base flow	$(x_0, x_{\text{end}}, N_x)$	$(\omega_{\min}, \omega_{\max}, N_\omega)$	$(\beta_{\min}, \beta_{\max}, N_\beta)$	$(y_{\min}, y_{\max}, N_y)$
Blasius	(300, 15000, 301)	(0.0005, 0.075, 240)	(0, 0.1, 50)	(0, 800, 101)
$Ma = 4.8$	(350, 10000, 500)	(0.0005, 0.1, 175)	(0, 0.13, 66)	(0, 400, 200)



TABLE I. An overview of discretization details for LST.

FIG. 4. Stability diagrams in the $x - F - \beta$ space for (a) The Blasius base flow and (b) the Mach 4.8 flat-plate hypersonic boundary layer.

III. RESULTS

A. In Fourier space

Prior to performing the analysis in physical space (x, t, z, y) , the LST solution is computed in the spectral domain $(x, \omega, \beta; y)$. The computational grid configuration is summarized in Table I, which outlines the range and number of points for each variable. Only non-negative values of the spanwise wavenumber β are tabulated, with the corresponding negative components reconstructed via the real-valued symmetry condition. In the wall-normal (y) direction, an adaptive Chebyshev grid is adopted to effectively capture variations in boundary layer thickness, while uniform grids are employed in the remaining directions. For compressible flow analyses – especially in hypersonic regimes – enhanced resolution in the wall-normal direction is often necessary to resolve steep gradients associated with instability. The grid configuration used in this study has been verified for grid independence to ensure numerical accuracy.

Figure 4 presents the stability diagram, highlighting the isosurface of $\alpha_i = 0$ (the neutral surface), along with cross-sectional views in the $x - F$ plane depicting the spatial distribution of the growth rate. The global frequency is defined as $F = \omega/Re$. For incompressible Tollmien–Schlichting (T–S) waves, the most significant growth occurs at $\beta = 0$, as shown in Figure 4(a). In the Mach 4.8 case, the second-mode instability exhibits a higher growth rate, although its unstable frequency band is comparatively narrower. The emergence of this mode is attributed to the existence of multiple solutions in the inviscid governing equations at hypersonic speeds [11].

Based on equation (6), a specific frequency is selected for the subsequent analysis. For the Blasius base flow, the frequency $F = 23 \times 10^{-6}$ yields the maximum N -factor at $\beta = 0$. By fixing F at this value, the stability diagram in the $x - \beta$ plane is obtained, as shown in Figure 5(a). For the Mach 4.8 case, three representative frequencies are considered, corresponding to distinct instability scenarios: (i) only the first instability mode is present at $F = 24 \times 10^{-6}$ (Figure 5(b)); (ii) both the first and second modes coexist at $F = 135 \times 10^{-6}$, with the first mode growing upstream of the second (Figure 5(c)); and (iii) only the second mode appears at $F = 179 \times 10^{-6}$ (Figure 5(d)).

B. Feature collection in physical space

The Fourier-space disturbance data presented in Section III A are transformed into physical space using Equation (4). The resulting dataset complies with the sampling theorem, guaranteeing that each wavelength is represented by at least two sampling points. For instance, in the x -direction, the incompressible case features wavelengths in the range $\lambda \in [110.05, 2795.00]$ with a spatial resolution of $\Delta x = 49.00$, whereas in the hypersonic case, the wavelengths

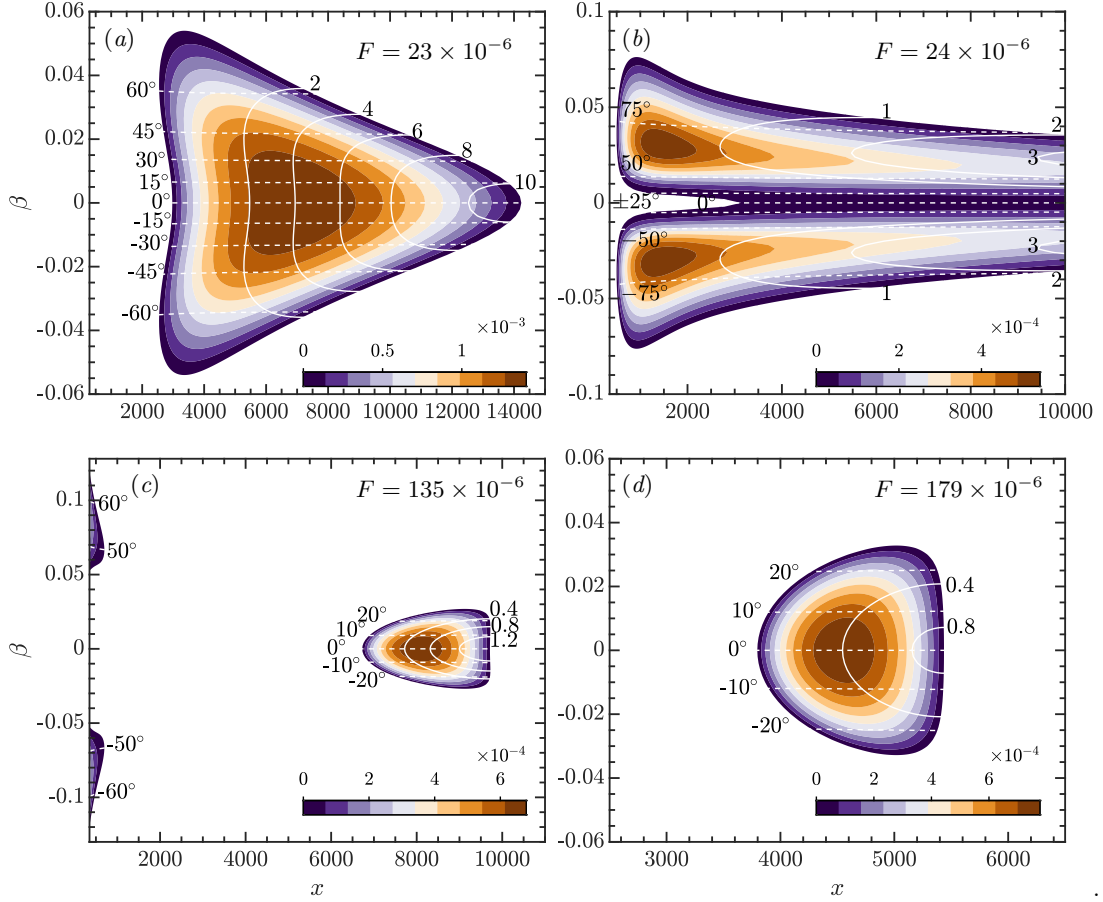


FIG. 5. Stability diagrams in the $x - \beta$ plane for (a) the Blasius boundary layer and (b-d) the Mach 4.8 boundary layer at a specified frequency. Solid white lines denote N -factor contours, and dashed white lines indicate wave angle ($\phi = \arctan(\beta/\alpha_r)$) contours.

span $\lambda \in [54.87, 1.71 \times 10^6]$ with $\Delta x = 19.34$. At this point, the spatial structure of the disturbances can be effectively visualized through crd₃ sectional slices in multiple dimensions.

Taking the Blasius base flow as an illustrative example, the disturbance field at a fixed wall-normal height is shown in Figure 6(a). To better understand the mechanism driving pattern formation, the contributions of individual β modes are analyzed. At small x locations, the amplitudes of various β modes are primarily governed by the external perturbation, and their superposition produces small-radius “ripples.” As x increases, modes with β values close to zero experience more rapid amplification and begin to dominate the disturbance structure. This selective amplification mechanism leads to an increase in the ripple radius in the downstream direction.

To reveal the spatial structure, additional visualizations in the $y-z$ and $x-y$ planes are provided in Figure 6, showing that the disturbances remain largely confined within the boundary-layer region. It is important to note that nonlinear effects become significant when disturbance amplitudes grow excessively. To account for this and ensure that most of the perturbations remain within the linear regime, the disturbances are rescaled prior to superposition, limiting their peak magnitude to 10% of the base flow velocity (normalized by the freestream velocity). This scaling helps constrain the influence of the initial disturbance amplitude on the subsequent evolution.

In addition to the streamwise-velocity components, other flow variables are visualized in Figure 7(a). The results show that the spatial structures of \tilde{u} , \tilde{v} , and \tilde{p} are qualitatively similar, exhibiting differences primarily in amplitude rather than in form. Furthermore, as illustrated in Figure 7(b), slices taken at different wall-normal heights reveal structurally consistent disturbance patterns. Notably, the spatial distribution of the maximum disturbance amplitudes across the wall-normal direction closely resembles the eigenvector profiles obtained from linear stability analysis.

The structural consistency among disturbance components is further confirmed in the hypersonic flow case, as illustrated in Figure 8(a), which corresponds to a frequency where only the second mode exhibits instability. In this scenario, a characteristic “rope-like” structure [36] emerges in the $x-y$ plane, most prominently in the density and temperature perturbations, as shown in Figure 8(b). This behavior is attributed to the wall-normal distribution of

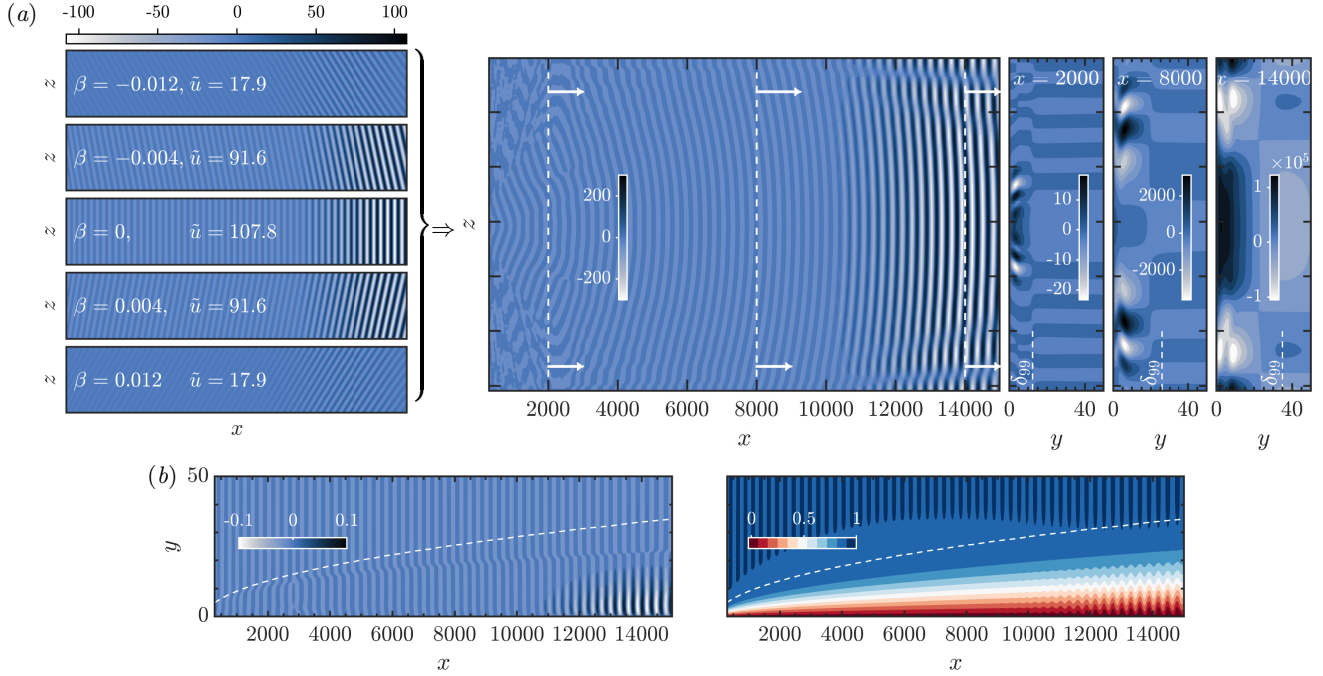


FIG. 6. Two-dimensional slices of the streamwise disturbance component \tilde{u} in physical space. (a) Middle panel: $x-z$ plane slice near the wall; left panel: corresponding single- β mode contribution; right panel: $y-z$ plane slice extracted along the dashed line in the middle panel. (b) $x-y$ plane slice at the disturbance centerline ($z = z_c$). The white dashed line indicates the boundary layer thickness. The left panel shows the disturbance component \tilde{u} , while the right displays the instantaneous velocity field ($\tilde{u} + U$).

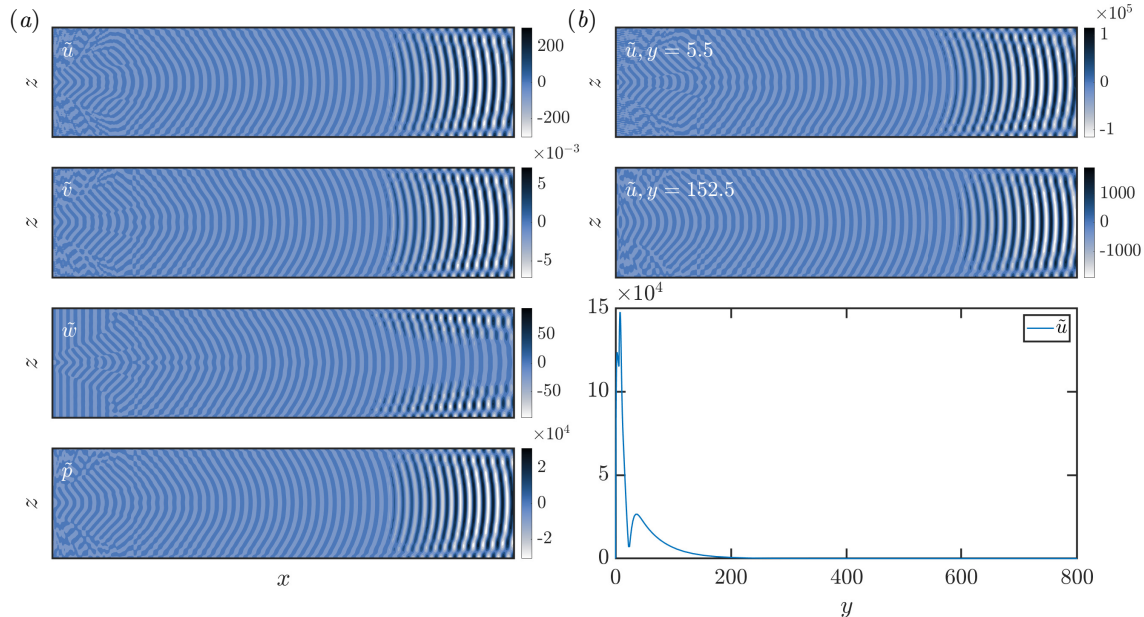


FIG. 7. The Blasius case. (a) Comparison of different disturbance components in the $x-z$ plane near the wall. (b) Distribution of the streamwise disturbance component \tilde{u} in the $x-z$ plane at different wall-normal heights. The bottom panel illustrates the variation of the maximum \tilde{u} amplitude in the $x-z$ plane as a function of y .

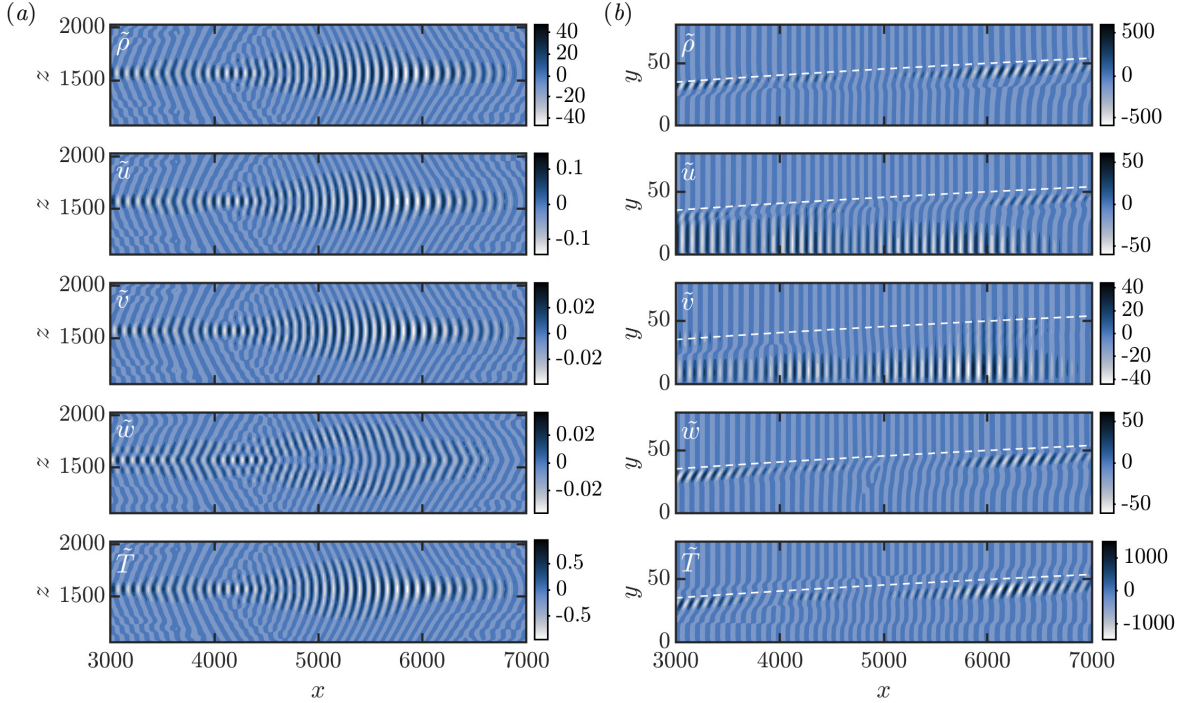


FIG. 8. The $Ma = 4.8$ case. (a) Comparison of different disturbance components in the x - z plane near the wall. (b) Distribution of disturbances in the x - y plane at the spanwise location $z = z_c$. The white dashed line denotes the boundary layer thickness.

the corresponding eigenvector associated with the second-mode instability.

We investigate the impact of external perturbations through the isosurfaces of \tilde{u} shown in Figure 9, which depict the disturbance field in three-dimensional space. The baseline case, characterized by $f = f_1$, $R = 200$, and a single disturbance source, corresponds to the results presented in Figures 6 and 7. When the frequency of the external perturbation is increased to $F = 41 \times 10^{-6}$ – a 76% increase compared to the baseline – the resulting disturbance field is illustrated in Figure 9(b). At this elevated frequency, the amplitude of the disturbance decreases, showing an initial growth followed by decay. This behavior is attributed to a reduced growth rate and a narrower instability band.

Regarding the spatial configuration of the external excitation, variations in the source setup do not necessarily lead to distinct disturbance evolution patterns. For instance, altering the form of the disturbance—by switching to f_2 or increasing the source radius to $R = 400$ – modifies the initial amplitude in Fourier space (as shown in Figure 2). The corresponding disturbance structures are depicted in Figures 9(c) and 9(d), respectively. In both cases, the influence of the modified source remains localized upstream, close to the disturbance origin. In other words, the exponential amplification of disturbances downstream dominates over the initial source modifications. Furthermore, when the original disturbance function is retained but two identical-frequency sources are symmetrically placed along the z -axis, the resulting structure – shown in Figure 9(e) – exhibits wave superposition and interference. These interactions give rise to new and more complex patterns in the disturbance field.

Recall figure 5, under hypersonic conditions, different frequencies give rise to distinct combinations of instability modes. We begin by examining the low-frequency case, where only the first-mode instability is active. Although this mechanism is analogous to that in incompressible flows, the dominant spanwise wavenumber shifts from $\beta = 0$ to finite β , resulting in oblique waves that form a characteristic “waffle-like” pattern near the centerline ($z = z_c$) of the disturbance field (Figure 10(a)).

As the frequency increases, the flow enters a regime where both first- and second-mode instabilities coexist. In this case, the first-mode instability develops in the upstream region, followed by a mild attenuation of the disturbance amplitude. As the flow progresses downstream into the second-mode instability region, the disturbance is re-amplified, as illustrated in Figure 10(b). Interestingly, for the frequency considered here, the overall disturbance amplitude does not exhibit a pronounced decay after exiting the first-mode unstable region. This behavior is attributed to the fact that attenuation primarily affects high- β components, which possess relatively low initial amplitudes. In contrast, low- β components maintain nearly constant amplitudes and thus continue to dominate the total disturbance field.

At higher frequencies, the flow becomes dominated exclusively by the second-mode instability, as shown in Figure 10(c). Before entering the unstable region, the disturbance amplitude remains nearly constant, reflecting the

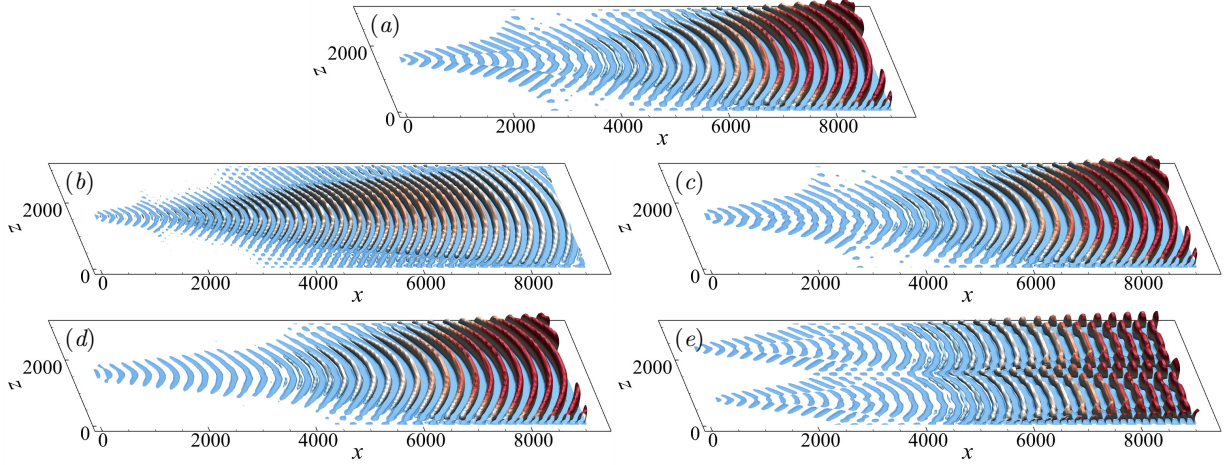


FIG. 9. Three-dimensional isosurfaces of the streamwise disturbance component \tilde{u} for the Blasius base flow, colored by the wall-normal coordinate y . (a) Reference configuration with $f = f_1$, $R = 200$, and a single source. (b) Case with a 76% higher frequency compared to the reference. (c) Case with a different perturbation function, $f = f_2$. (d) Case with increased perturbation radius, $R = 400$. (e) Case involving two disturbance sources instead of one.

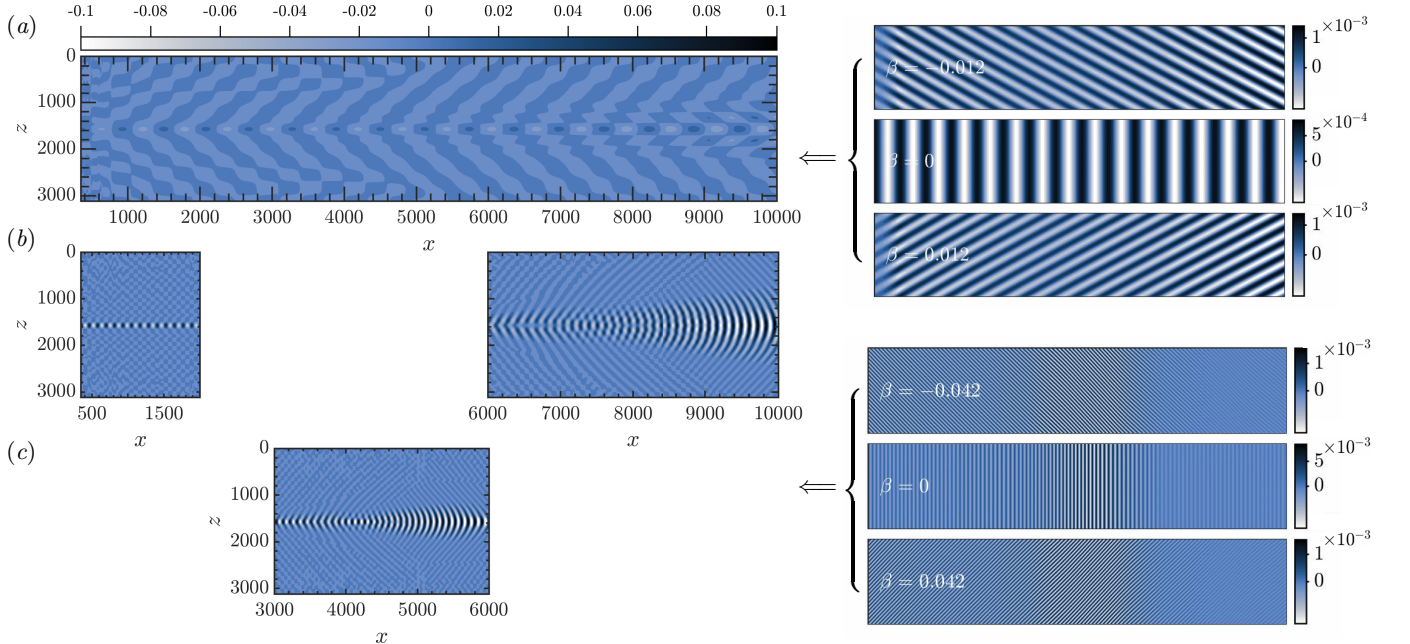


FIG. 10. Physical disturbance structures near the wall ($y \rightarrow 0$) at different frequencies for the $Ma = 4.8$ case, corresponding to the Fourier-space results shown in Figure 5(b-d). (a) Instability field dominated exclusively by the first mode. (b) Disturbance structure in a regime where first-mode and second-mode instabilities coexist, appearing in the upstream and downstream regions, respectively. (c) Instability field dominated solely by the second mode.

spatial characteristics of the externally imposed forcing. As the flow approaches the lower branch of the neutral stability curve, components with small spanwise wavenumbers ($\beta \rightarrow 0$) begin to amplify more rapidly and eventually dominate the disturbance field. This selective growth leads to a gradual reorganization of the disturbance structure into a “shield-like” pattern, characterized by the predominance of two-dimensional waves – similar to the behavior observed in Figure 7(a).

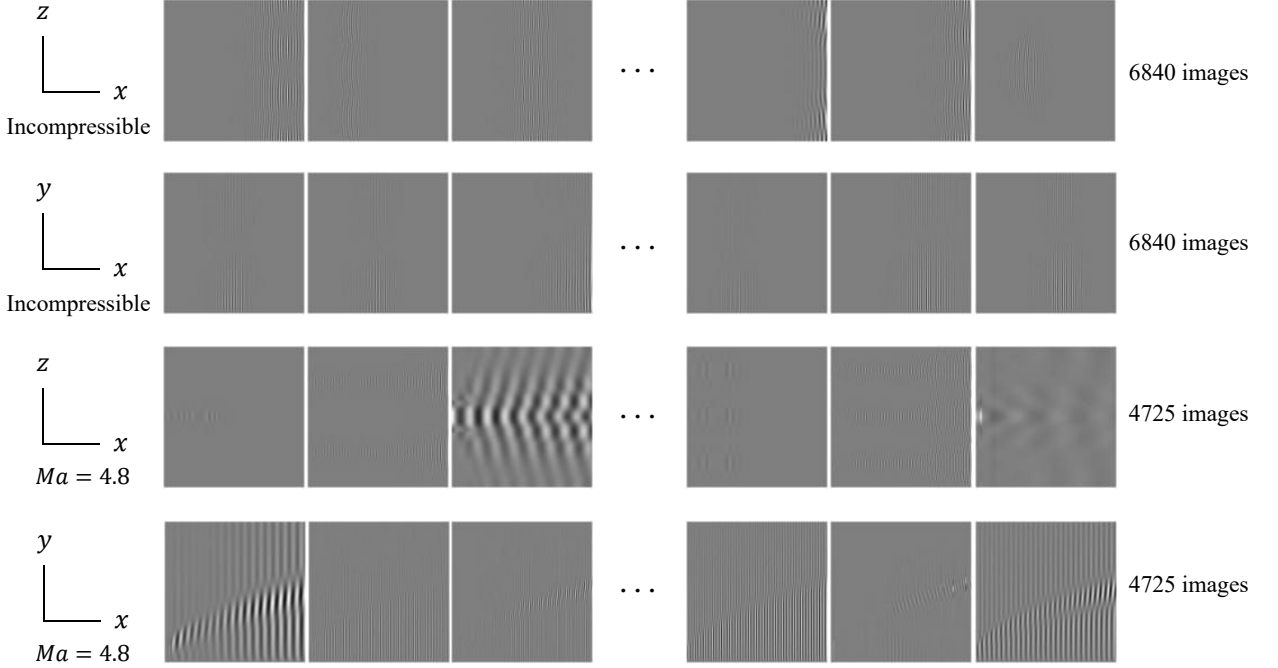


FIG. 11. Sample images of the flow field.

C. Data-driven N -factor prediction

In this study, a CNN model is employed to predict flow instability characteristics, using slices of the streamwise velocity disturbance component \tilde{u} (e.g., Figure 6 and Figure 10) as input and the corresponding N -factor as output. The N -factor, in this context, is defined as a function of x and ω , as shown in Figure 5, and is determined by selecting the maximum amplification among all spanwise wavenumbers β at each streamwise location. Accordingly, for each x - z or x - y slice, the model predicts the N -factor distribution along the streamwise direction x .

Guided by the observation in the Fourier-space data (Figure 5(a)), the frequency range F for the incompressible case is chosen between 6.7×10^{-6} and 56.7×10^{-6} , discretized into 240 uniformly spaced points. For each frequency, two types of input images are generated: one corresponding to the x - z plane near the wall, and the other to the x - y plane taken at the disturbance centerline z_c . For the $Ma = 4.8$ case, 175 frequency points are specified over the F range between 1.4×10^{-6} and 285.7×10^{-6} . To enhance the visualization and learning of disturbance structures, the wall-normal extent of the x - y images is determined based on the boundary layer thickness at the downstream end of the domain (x_{\max}), which is approximately 35 for the Blasius boundary layer and 100 for the $Ma = 4.8$ case.

In addition to frequency discretization, dataset diversity is further enhanced through parametric variations in the disturbance configuration. Specifically, three distinct perturbation functions, three disturbance radii, and three different source-numbers are considered, as summarized in Figure 2. These combinations yield a total of 27 unique disturbance configurations. When combined with the frequency samples – 240 for the incompressible case and 175 for the compressible ($Ma = 4.8$) case – this results in 6,480 and 4,725 image samples, respectively, across the two base flows and both slicing orientations (x - z and x - y planes). The complete set of samples forms the image-based dataset used in this study, as shown in Figure 11.

The generated disturbance pattern dataset was used to train and evaluate a CNN model, with samples partitioned into training, validation, and test sets in a 70%:15%:15% ratio. Hyperparameter tuning was performed via random search using the validation set. The explored parameter ranges included: learning rate $\in [0.0001, \mathbf{0.001}, 0.01]$, batch size $\in [16, \mathbf{32}, 64]$, dropout rate $\in [0.1, \mathbf{0.2}, 0.3, 0.4, 0.5]$, and activation function $\in [\text{ReLU}, \text{Leaky ReLU}]$. A total of 20 independent hyperparameter combinations were sampled and evaluated using the mean squared error as the performance metric. The configuration yielding the lowest validation error—highlighted in bold above—was selected for final model training and testing.

After training and validation, the model's performance was assessed on the test set. Figure 12 presents prediction results for four representative samples in the x - z plane from the incompressible case. Figure 12(a) shows the Grad-CAM visualizations, which highlight the regions in the input image that most strongly influence the CNN's prediction

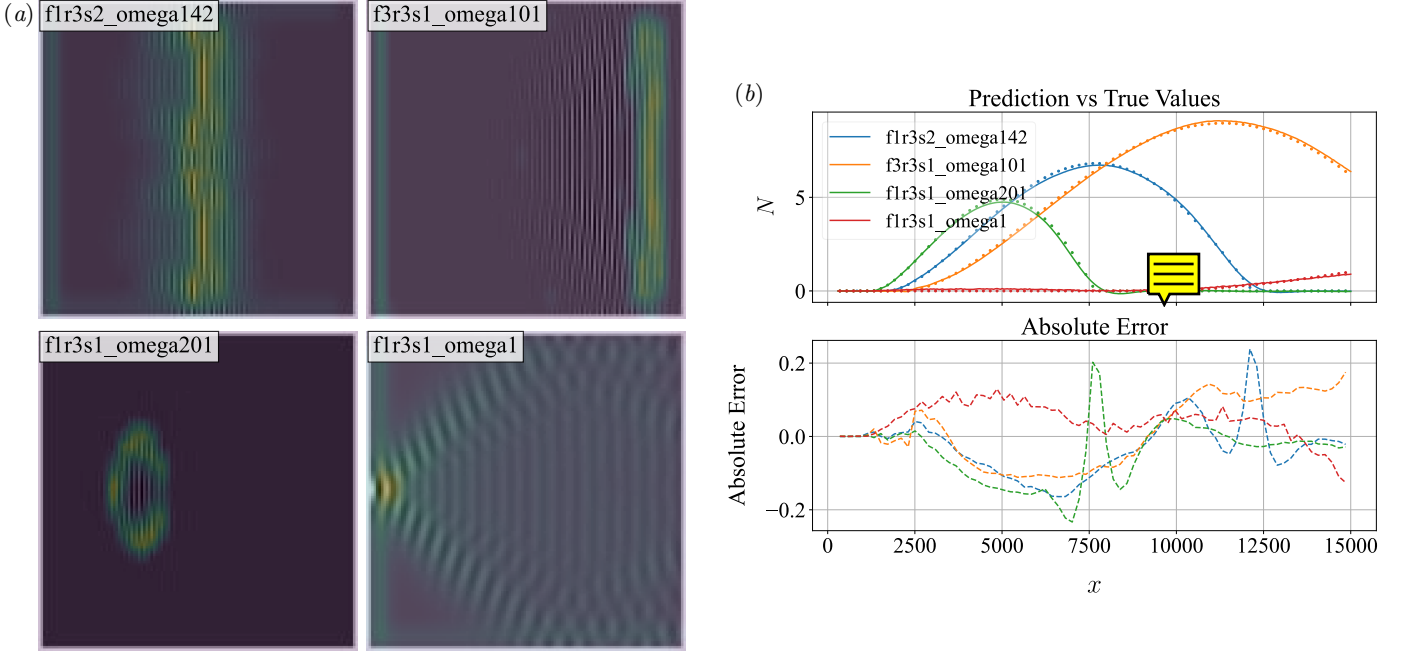


FIG. 12. Prediction performance of the CNN model. (a) Visualization of representative test samples, with predicted heatmaps overlaid on the original input images. (b) Comparison of CNN predictions and corresponding errors against the ground truth.

by leveraging the gradients of the target output with respect to the feature maps. The resulting heatmaps reveal that the most activated regions are concentrated around the T-S wave structures, indicating that the model has effectively captured the key flow features responsible for instability growth. Each subfigure is labeled in the upper-left corner with a descriptor of the corresponding input sample. For example, “f1r3s2_omega142” refers to a configuration with $f = f_1$, $R = 400$ (i.e., the third radius setting), two disturbance sources, and a frequency index of 142. Figure 12(b) compares the CNN-predicted N -factors (solid lines) with LST-computed reference values (circular markers) for corresponding samples, while the lower panel quantifies the prediction error. As evident from the plots, the CNN predictions closely follow the LST results, demonstrating strong agreement and high predictive accuracy.

To assess the overall generalizability of the model, the mean absolute error (MAE) across all test samples is statistically summarized in the form of a histogram, as shown in Figure 13. The model demonstrates strong predictive performance, with the majority of errors falling within $\Delta N = \pm 0.2$. To investigate the improvement in performance brought by the optimized neural network, we experimented with several of the models discussed in Section II C, and the results are provided in Appendix A. These models showed enhanced performance on the test set, reducing the median error of the N -factor to 0.028.

It is worth noting that the image dataset used in this study was generated from linear stability theory (LST), which serves as a reduced-order model for physical disturbances in the linear regime. However, we expect that similar predictive performance could be achieved using flow visualizations derived from experimental observations or measurements. For example, prediction frameworks based on temperature-sensitive paint (TSP), pressure-sensitive paint (PSP), oil-flow visualization, particle image velocimetry (PIV), or laser-induced fluorescence (LIF), combined with appropriate data assimilation or preprocessing techniques, could be developed. These techniques allow for the creation of diverse models tailored to different types of experimental or diagnostic data, thereby broadening the applicability and flexibility of the dataset.

IV. CONCLUSION

Building on the success and wide applicability of linear stability theory (LST), this study extends its use beyond the traditional prediction of growth rates and dispersion relations from detailed stability diagrams. By incorporating machine learning, LST is employed to generate perturbation data in Fourier space, which are then transformed into physical space through the matching of predefined external source distributions. In this way, large-scale flow instability datasets are constructed, providing a foundation for mode identification and transition prediction in engineering

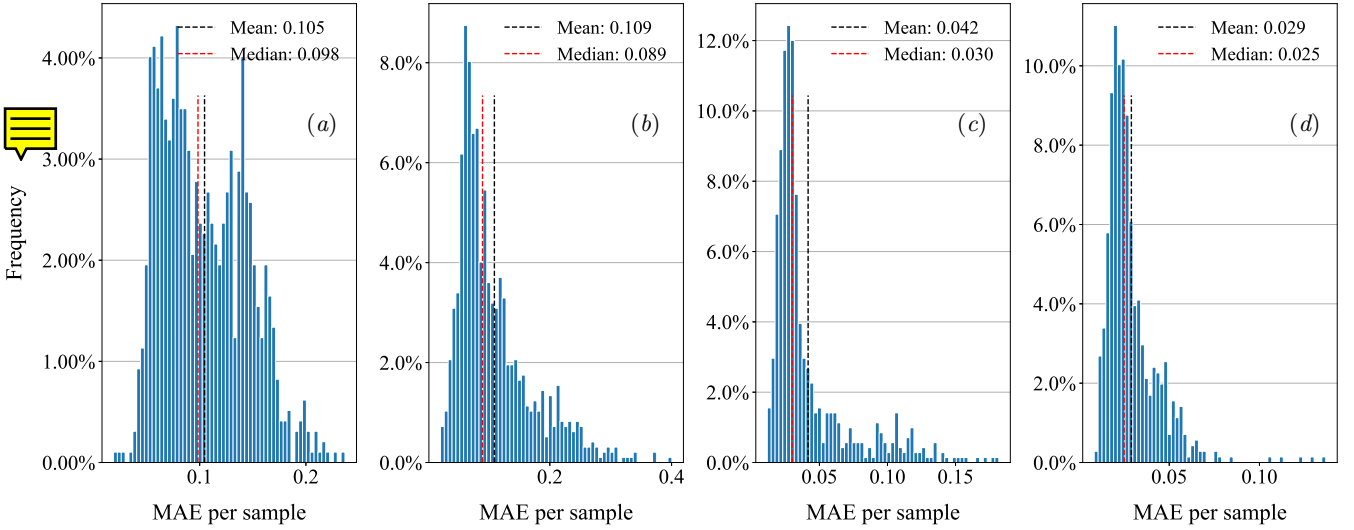


FIG. 13. MAE distribution of CNN model predictions across all test set samples. The horizontal axis denotes the error magnitude, and the vertical axis indicates the frequency of occurrence. Subplots correspond to: (a) incompressible case in the $x-z$ plane, (b) incompressible case in the $x-y$ plane, (c) hypersonic case in the $x-z$ plane, and (d) hypersonic case in the $x-y$ plane.

applications. The flows examined in this study include flat-plate boundary layer flows in both incompressible and hypersonic regimes. External perturbations are introduced as point sources, with their characteristics determined by the chosen perturbation functions and the number of sources.

Perturbation structures and characteristic patterns are extracted through systematic analysis of the generated datasets. The results indicate that disturbances remain confined within the boundary layer, with dominant structures appearing either near the wall or close to the boundary-layer edge, denoted by δ_{99} . A comprehensive spatial examination reveals that perturbations exhibit similar patterns in the $x-z$ plane, largely independent of their physical components or wall-normal position, with variations manifesting primarily in amplitude. In the hypersonic regime, the coexistence of Mack's first and second modes leads to a transition from oblique wave-dominated growth (first mode) to downstream planar wave dominance (second mode). Correspondingly, the perturbation structures evolve from staggered arrangements along the spanwise (z) direction to “shield-like” patterns dominated by two-dimensional waves. These characteristic patterns are normalized and assembled into an image dataset that closely resembles experimental or in-flight visualizations.

Integrating data-driven methodologies, this study further employs a CNN model to predict N -values directly from perturbation patterns. The results demonstrate that prediction errors are predominantly within ± 0.2 , confirming the model's high accuracy and robustness. To further utilize the outcome of the proposed method, one can combine the N -factor prediction with amplitude measurements at an upstream position, such that the perturbation amplitude can be estimated and calibrated with the transitional value (e.g., 1% for T-S waves), offering a novel pathway for rapid identification of transition locations based on flow visualization.

Future work will focus on extending this framework to more complex flow conditions, such as variable boundary conditions and multi-mode interactions, to further enrich the dataset and enhance model generalizability. Investigating the nonlinear evolution of disturbances will also be a key direction, offering deeper insights into transition mechanisms and the prediction of transition onset.

Appendix A: Performance Comparison of Different CNN Models

Taking the test results on the incompressible $x-z$ plane as an example, we compare our proposed CNN architecture with several widely used models, including AlexNet, ResNet-18, and ConvNeXt-Tiny. Minor modifications were made to these architectures to adapt them for regression tasks. The quantitative comparison is shown in Table II. The results indicate that, the custom CNN employs a lightweight convolutional design yet incorporates large fully-connected layers, resulting in the highest number of parameters while maintaining relatively low FLOPs. AlexNet shows a slight performance improvement over the custom CNN. ResNet achieves a good balance between parameter count and performance, offering a favorable trade-off. ConvNeXt, as a modern architecture, exhibits the strongest

Model	Parameters	FLOPs	Mean error	Median error
custom CNN (figure 3)	34.79M	155.3M	0.105	0.098
AlexNet	31.18M	659.1M	0.096	0.086
ResNet	11.32M	1.1G	0.053	0.046
ConvNeXt	28.04M	2.9G	0.031	0.028

TABLE II. Performance comparison of different CNN models.

representational capability among all models.

DECLARATION OF INTERESTS

The authors report no conflict of interests.

-
- [1] H. L. Reed, W. S. Saric, and D. Arnal, Linear stability theory applied to boundary layers, *Annual review of fluid mechanics* **38**, 389 (1996).
- [2] W. S. Saric, H. L. Reed, and E. B. White, Stability and transition of three-dimensional boundary layers, *Annual review of fluid mechanics* **35**, 413 (2003).
- [3] V. Theofilis, Global linear instability, *Annual Review of Fluid Mechanics* **43**, 319 (2011).
- [4] K. Taira, S. L. Brunton, S. T. Dawson, C. W. Rowley, T. Colonius, B. J. McKeon, O. T. Schmidt, S. Gordeyev, V. Theofilis, and L. S. Ukeiley, Modal analysis of fluid flows: An overview, *AIAA journal* **55**, 4013 (2017).
- [5] R. Govindarajan and K. C. Sahu, Instabilities in viscosity-stratified flow, *Annual review of fluid mechanics* **46**, 331 (2014).
- [6] J. Ren, O. Marxen, and R. Pecnik, Boundary-layer stability of supercritical fluids in the vicinity of the widom line, *Journal of Fluid Mechanics* **871**, 831 (2019).
- [7] X. Gloerfelt, J.-C. Robinet, L. Sciacovelli, P. Cinnella, and F. Grasso, Dense-gas effects on compressible boundary-layer stability, *Journal of Fluid Mechanics* **893**, A19 (2020).
- [8] X. Chen, L. Wang, and S. Fu, Energy transfer of hypersonic and high-enthalpy boundary layer instabilities and transition, *Physical Review Fluids* **7**, 033901 (2022).
- [9] H. Schlichting and K. Gersten, *Boundary-layer theory* (springer, 2016).
- [10] L. M. Mack, Linear stability theory and the problem of supersonic boundary-layer transition, *AIAA journal* **13**, 278 (1975).
- [11] L. M. Mack, Boundary-layer linear stability theory, *Agard rep* **709** (1984).
- [12] W. S. Saric *et al.*, Gortler vortices, *Annual Review of Fluid Mechanics* **26**, 379 (1994).
- [13] P. Hall, M. R. Malik, and D. Poll, On the stability of an infinite swept attachment line boundary layer, *Proceedings of the Royal Society of London. A. Mathematical and Physical Sciences* **395**, 229 (1984).
- [14] T. Herbert, Secondary instability of boundary layers, *Annual review of fluid mechanics* **20**, 487 (1988).
- [15] M. I. Zafar, H. Xiao, M. M. Choudhari, F. Li, C.-L. Chang, P. Paredes, and B. Venkatachari, Convolutional neural network for transition modeling based on linear stability theory, *Physical Review Fluids* **5**, 113903 (2020).
- [16] P. C. Di Leoni, L. Lu, C. Meneveau, G. E. Karniadakis, and T. A. Zaki, Neural operator prediction of linear instability waves in high-speed boundary layers, *Journal of Computational Physics* **474**, 111793 (2023).
- [17] Z. Mao, L. Lu, O. Marxen, T. A. Zaki, and G. E. Karniadakis, Deepm&mnnet for hypersonics: Predicting the coupled flow and finite-rate chemistry behind a normal shock using neural-network approximation of operators, *Journal of computational physics* **447**, 110698 (2021).
- [18] H. Nie, W. Song, Z. Han, J. Chen, and G. Tu, A surrogate-based en method for compressible boundary-layer transition prediction, *Journal of Aircraft* **59**, 89 (2022).
- [19] J. Deng, W. Dong, R. Socher, L.-J. Li, K. Li, and L. Fei-Fei, Imagenet: A large-scale hierarchical image database, in *2009 IEEE conference on computer vision and pattern recognition* (Ieee, 2009) pp. 248–255.
- [20] A. Krizhevsky, I. Sutskever, and G. E. Hinton, Imagenet classification with deep convolutional neural networks, *Advances in neural information processing systems* **25** (2012).
- [21] V. Panayotov, G. Chen, D. Povey, and S. Khudanpur, Librispeech: an asr corpus based on public domain audio books, in *2015 IEEE international conference on acoustics, speech and signal processing (ICASSP)* (IEEE, 2015) pp. 5206–5210.
- [22] P. Rajpurkar, R. Jia, and P. Liang, Know what you don’t know: Unanswerable questions for squad, *arXiv preprint arXiv:1806.03822* (2018).
- [23] Y. Li, E. Perlman, M. Wan, Y. Yang, C. Meneveau, R. Burns, S. Chen, A. Szalay, and G. Eyink, A public turbulence database cluster and applications to study lagrangian evolution of velocity increments in turbulence, *Journal of Turbulence* , N31 (2008).

- [24] J. Jeong and F. Hussain, On the identification of a vortex, *Journal of fluid mechanics* **285**, 69 (1995).
- [25] H. Yao, P. Yeung, T. Zaki, and C. Meneveau, Forward and inverse energy cascade in fluid turbulence adhere to kolmogorov's refined similarity hypothesis, *Physical review letters* **132**, 164001 (2024).
- [26] R. Samtaney, D. I. Pullin, and B. Kosović, Direct numerical simulation of decaying compressible turbulence and shocklet statistics, *Physics of Fluids* **13**, 1415 (2001).
- [27] J. Ren, Y. Wu, X. Mao, C. Wang, and M. Kloker, Sensitivity of three-dimensional boundary layer stability to intrinsic uncertainties of fluid properties: a study on supercritical CO₂, *Journal of Fluid Mechanics* **1007**, A7 (2025).
- [28] J. Ren and M. Kloker, Instabilities in three-dimensional boundary-layer flows with a highly non-ideal fluid, *Journal of Fluid Mechanics* **951**, A9 (2022).
- [29] C. Stemmer, M. J. Kloker, and S. Wagner, Navier-stokes simulation of harmonic point disturbances in an airfoil boundary layer, *AIAA journal* **38**, 1369 (2000).
- [30] Y. LeCun, L. Bottou, Y. Bengio, and P. Haffner, Gradient-based learning applied to document recognition, *Proceedings of the IEEE* **86**, 2278 (1998).
- [31] K. Simonyan and A. Zisserman, Very deep convolutional networks for large-scale image recognition, *arXiv preprint arXiv:1409.1556* (2014).
- [32] K. He, X. Zhang, S. Ren, and J. Sun, Deep residual learning for image recognition, in *Proceedings of the IEEE conference on computer vision and pattern recognition* (2016) pp. 770–778.
- [33] M. Tan and Q. Le, Efficientnet: Rethinking model scaling for convolutional neural networks, in *International conference on machine learning* (PMLR, 2019) pp. 6105–6114.
- [34] Z. Liu, H. Mao, C.-Y. Wu, C. Feichtenhofer, T. Darrell, and S. Xie, A convnet for the 2020s, in *Proceedings of the IEEE/CVF conference on computer vision and pattern recognition* (2022) pp. 11976–11986.
- [35] J. Van Ingen, A suggested semi-empirical method for the calculation of the boundary layer transition region, University of Techn., Dept. of Aerospace Eng., Report UTH-74 (1956).
- [36] S. Laurence, A. Wagner, and K. Hannemann, Experimental study of second-mode instability growth and breakdown in a hypersonic boundary layer using high-speed schlieren visualization, *Journal of Fluid Mechanics* **797**, 471 (2016).